

UC Irvine

UC Irvine Previously Published Works

Title

Scattering-Angle-Resolved Optical Coherence Tomography of a Hypoxic Mouse Retina Model.

Permalink

<https://escholarship.org/uc/item/7gc254p0>

Authors

Gardner, Michael

Rahman, Ayesha

Milner, Thomas

et al.

Publication Date

2019

DOI


10.1177/1179069519837564

Copyright Information

This work is made available under the terms of a Creative Commons Attribution-NonCommercial License, available at <https://creativecommons.org/licenses/by-nc/4.0/>

Peer reviewed

Scattering-Angle-Resolved Optical Coherence Tomography of a Hypoxic Mouse Retina Model

Michael R Gardner^{1,2} , Ayesha S Rahman¹, Thomas E Milner¹ and Henry G Rylander III¹

¹Department of Biomedical Engineering, The University of Texas at Austin, Austin, TX, USA.

²Department of Chemical Engineering, University of Bahrain, Isa Town, Bahrain.

Journal of Experimental Neuroscience

Volume 13: 1–10

© The Author(s) 2019

Article reuse guidelines:

sagepub.com/journals-permissions

DOI: 10.1177/1179069519837564



ABSTRACT: Several studies have noted a correlation between retinal degeneration and traumatic encephalopathy (TE) making the retina a leading candidate for detection and assessment. Scattering-angle-resolved optical coherence tomography (SAR-OCT) is a candidate imaging modality to detect sub-resolution changes in retinal microstructure. SAR-OCT images of murine retinas that experience a hypoxic insult—euthanasia by isoflurane overdose—are presented. A total of 4 SAR-OCT measurement parameters are reported in 6 longitudinal experiments: blood flow volume fraction, total retinal thickness, reflectance index, and scattering angle. As each mouse expires, blood flow volume fraction decreases, total retinal thickness increases, reflectance index decreases, and scattering angle diversity increases. Contribution of the retinal vasculature to scattering angle diversity is discussed. Results of this study suggest the utility of SAR-OCT to measure TE using scattering angle diversity contrast in the retina.

KEYWORDS: Optical coherence tomography, angle-resolved imaging, mouse, retinal imaging, hypoxia

RECEIVED: October 26, 2018. **ACCEPTED:** February 21, 2019.

TYPE: Traumatic Brain Injury (TBI) and Chronic Traumatic Encephalopathy (CTE) - Original Research

FUNDING: The author(s) disclosed receipt of the following financial support for the research, authorship, and/or publication of this article: This research was supported by a grant from The University of Texas System Neuroscience and Neurotechnology Research Institute and the Cancer Prevention Research Institute of Texas (DP 150102). M.R.G. was

supported by the NIH T32 training grant EB007507 and is currently supported as a Fulbright Scholar by the US Department of State, hosted at the University of Bahrain.

DECLARATION OF CONFLICTING INTERESTS: The author(s) declared no potential conflicts of interest with respect to the research, authorship, and/or publication of this article.

CORRESPONDING AUTHOR: Michael R Gardner, Department of Biomedical Engineering, The University of Texas at Austin, 107 W Dean Keeton Street, Austin, TX 78712, USA. Email: mgardner@utexas.edu

Introduction

Clear and quantifiable measures of traumatic encephalopathy (TE) are prerequisite to the design of clinical trials to test TE pharmacologic intervention. The eye is a window to the brain as the optic nerve is anatomically a tract of the brain and the retinal ganglion cells (RGCs), the axons of which form the retinal nerve fiber layer (NFL), project primarily to the lateral geniculate nucleus of the thalamus.¹

Patients with concussion frequently report visual symptoms. Some symptoms and signs of mild TE include increased light sensitivity, loss of visual acuity and decreased contrast sensitivity, poor color discrimination, visual field defects, nystagmus, diplopia and visual pursuit disorders, accommodative convergence insufficiency, loss of accommodation, difficulty reading, and defects in binocular stereoacuity. Zonner et al² reported that the near point of convergence can be perturbed over the long term by subconcussive head impacts but may normalize over time. Elbin et al³ studied vestibular and ocular motor impairment following concussion in athletes and found that optokinetic nystagmus was a biomarker for concussion injury.

Pathological studies of eyes of retired athletes who have died with chronic traumatic encephalopathy (CTE) have suggested retinal thinning in addition to brain atrophy known to occur in athletes with a history of multiple concussions/head traumas. Ann McKee and Alosco⁴ discussed ocular biomarkers of head injury. Animal models of blast injury also demonstrate macular RGC thinning over time following injury.^{5,6} The retinal NFL contains RGC axons that degenerate in patients with neurologic and neurodegenerative disorders, including glaucoma,

multiple sclerosis, and Alzheimer disease. Optical coherence tomography (OCT) is a high-resolution, non-invasive imaging technique used regularly in ophthalmology; OCT ophthalmic systems use near-infrared light (800–1100 nm) to measure the thickness of retinal sublayers. Retinal nerve fiber layer thickness (NFLT) measured with OCT has been demonstrated to be abnormal in traumatic optic neuropathy^{7,8} and it is suggested that OCT may be applicable to evaluate RGC loss in TE.

Our group has investigated the application of scattering-angle-resolved optical coherence tomography (SAR-OCT) as a field-deployable approach to investigate optic nerve structure associated with neurodegeneration. Preliminary evidence based on glaucoma suspect eyes has shown that NFL reflectance is the earliest detectable measure of optic nerve dysfunction (before NFLT changes).⁹ A new measure, normalized reflectivity index (NRI), was introduced to quantify the NFL reflectance changes observed in early glaucoma.¹⁰ NRI can be determined from images obtained with conventional commercial ophthalmic OCT systems. Novel instrumentation, SAR-OCT, was then constructed to quantify backscattered light angle anisotropy associated with NFL reflectance change.^{11–13}

The pathophysiology of traumatic brain injury (TBI) is believed to involve the brain's vascular structural integrity. Kamp et al¹⁴ assessed cortical perfusion in patients suffering severe TBI using intraoperative indocyanine green (ICG) imaging. Patients with an unfavorable clinical outcome showed an altered shape of the ICG-derived fluorescence curve, a faster



increase of the ICG-derived fluorescence intensity in the cortical arteries, and a significantly greater residual fluorescence intensity. Ischemia, capillary leakage, and venous congestion are likely correlates of TE.

The mouse eye is remarkably similar to the human eye and is commonly studied with OCT for preclinical research. Previous publications with rodent retinal models report a variety of features including those related to retinal layer thickness,^{15–17} angiographic analysis,^{18–20} spectroscopic variation,^{21,22} and polarization.^{23,24}

The purpose of this investigation is to report the earliest observed changes detected by SAR-OCT in neurodegeneration induced by ischemia in a murine model. This investigation is not designed to emulate TE but rather to introduce and investigate the use of SAR-OCT in ischemic neurodegeneration. One aim of this study is to demonstrate the capability of SAR-OCT into detecting scattering angle changes in the murine retina following a hypoxic insult. Mice are euthanized via isoflurane overdose while the retina is imaged using a customized SAR-OCT system. Experiments investigate the sensitivity of SAR-OCT to characterize scattering angle changes in longitudinal studies by demonstrating shifts in scattering angle distributions and reflectance index fluctuations.

Materials and Methods

Animal protocol

This study adheres to ARVO guidelines on animal research (IACUC protocol #AUP-2015-00156). A total of 6 B6SJL F1/J mice were obtained from the Jackson Laboratory (JAX stock #100012) at age 10 weeks. Each mouse was initially anesthetized in an induction chamber (3% mg/kg isoflurane). Once recumbent, the animal was gently removed from the chamber, placed in a secure stereotaxic mount, and continued to receive anesthesia via a custom nose cone (isoflurane, 0.5%–3%).

The animal's left pupil was dilated with 1 drop of tropicamide (Mydrum). Subsequently, the eye was covered with a drop of hydroxypropyl methylcellulose solution (Methocel 2%) for index matching to the SAR-OCT system's objective, and a fundus lens was brought into contact with the mouse cornea. A hydroxypropyl methylcellulose solution was applied to the right eye to protect the cornea.

After recording a series of baseline anesthetized murine SAR-OCT retinal images over 10 to 20 minutes (imaging at intervals of approximately 4 minutes), the isoflurane concentration was increased to 5% to initiate hypoxia. SAR-OCT images were recorded for approximately 1 hour after oxygen deprivation was initiated, well after the mouse had expired and until corneal clouding began to degrade image quality.

Instrumentation

A previously reported customized SAR-OCT system was used for this study (Figure 1).^{12,13} The SAR-OCT system is

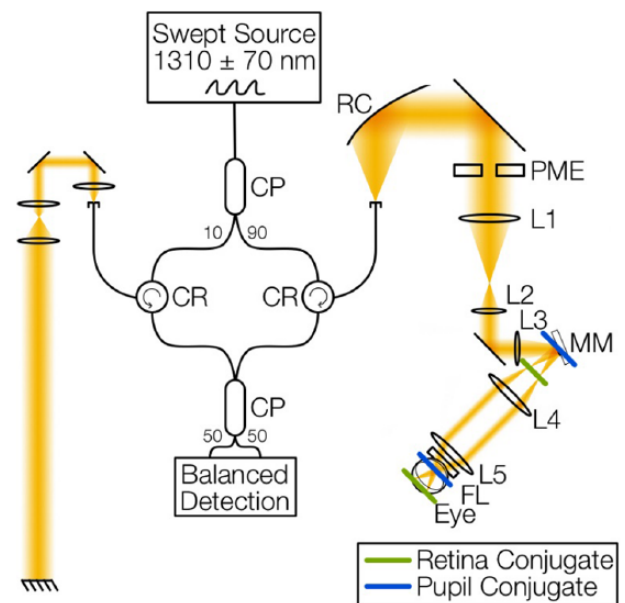


Figure 1. Customized SAR-OCT system for murine retinal imaging. The SAR-OCT system includes a 1310 nm \pm 70 nm swept-source laser and a fiber-based interferometer (CP: fiber coupler, CR: fiber circulator). The sample arm includes a reflective collimator (RC), path length multiplexing element (PME), several gradient index lenses (L1–L5), a dual-axis microelectromechanical system mirror (MM) conjugate to the ocular pupil plane, and a fundus lens (FL) that interfaces with the mouse cornea. The reference arm includes 3 lenses for dispersion compensation and a mirror path length matched to the mouse's retina. Source: Reproduced with permission from Gardner et al.¹² SAR-OCT, scattering-angle-resolved optical coherence tomography.

a swept-source fiber-based system and operates at a center wavelength of 1310 nm (140 nm bandwidth, 100 kHz repetition rate, 15 mW average power). The SAR-OCT system has an axial resolution of 11.7 μ m and a lateral resolution of 24.0 μ m in air.

A translating lens (L3) controls for changes in the focal plane due to ocular power variation between mice, and a fundus lens enables a tighter spot size on the retina. A dual-axis microelectromechanical system (MEMS) mirror (Mirrorcle Technologies, Inc) allows for ocular pupil plane beam pivoting.

An integral component of the SAR-OCT system is a path length multiplexing element (PME), described in detail by Yin et al,²⁵ Wang et al,¹¹ and Gardner et al¹³ The PME provides additional contrast to standard OCT images by separating sample path light into 3 different path lengths, each corresponding to a different angular range. Path length 1 (L_1 ; “Low”) is light that has scattered at generally low angles, whereas path lengths 2 (H_2 ; “High 2”) and 3 (H_3 ; “High 3”) contain light that has scattered at generally higher angles (Figure 2A).

Each B-scan location was collected 8 times sequentially for angiographic analysis. The B-scans are averaged across the 8 repeating B-scans and across each of the 3 path lengths for improved signal-to-noise ratio (SNR; Figure 2B). This processing rendered retinal volumes (150 \times 512 \times 512 voxels).

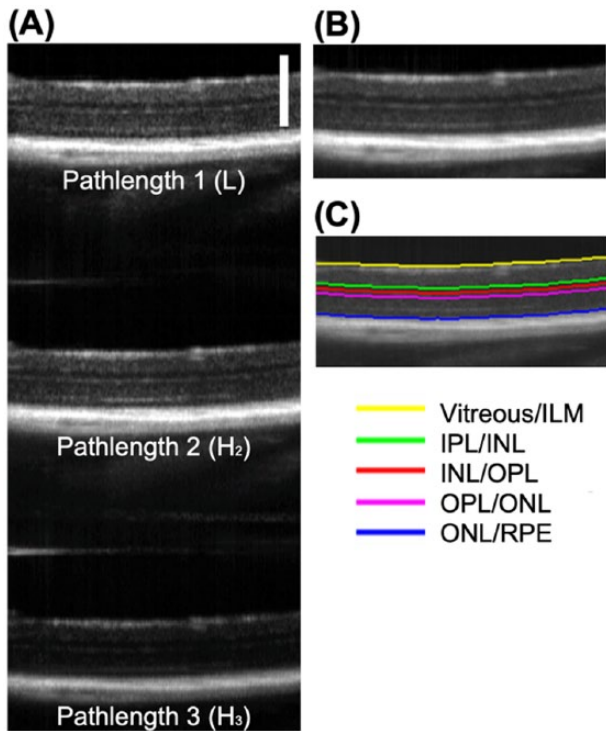


Figure 2. (A) Native path-length-multiplexed SAR-OCT image contains 3 sub-images with different path lengths (L , H_2 , and H_3). The path lengths may be averaged to obtain a single OCT retinal image (B). The averaged retinal image is segmented using a custom semi-automatic algorithm (C). The axial scale bar is $300\mu\text{m}$; the lateral field of view is 1.3mm (37°). ILM, internal limiting membrane; INL, inner nuclear layer; IPL, inner plexiform layer; ONL, outer nuclear layer; OPL, outer plexiform layer; RPE, retinal pigment epithelium; SAR-OCT, scattering-angle-resolved optical coherence tomography.

A custom semi-automatic retinal segmentation algorithm¹³ based on Sobel edge detection²⁶ distinguishes 5 retinal layer interfaces (Figure 2C): (1) vitreous/internal limiting membrane (ILM), (2) inner plexiform layer (IPL)/inner nuclear layer (INL), (3) INL/outer plexiform layer (OPL), (4) OPL/outer nuclear layer (ONL), and (5) ONL/retinal pigment epithelium (RPE). Other retinal layers are not segmented.

Data analysis

For each mouse, 4 measurement parameters were computed: (1) blood flow volume fraction, (2) total retinal thickness, (3) reflectance index, and (4) scattering angle. Each is described below.

Blood flow volume fraction. To probe murine retinal perfusion status (life or death), blood flow was monitored using complex differential variance, which intrinsically limits phase noise due to bulk motion.²⁷ The 3 murine vascular plexuses were identified using the retinal layer segmentation algorithm (based on native scattering properties), and each vascular plexus was max-projected to an en face image. Retinal blood vessels were then binarized by a semi-custom filtering process. After Frangi filtering for improved vessel detection,²⁸ a histogram equalization step was implemented. Parameters used for adaptive histogram equalization were averaged over each mouse in the

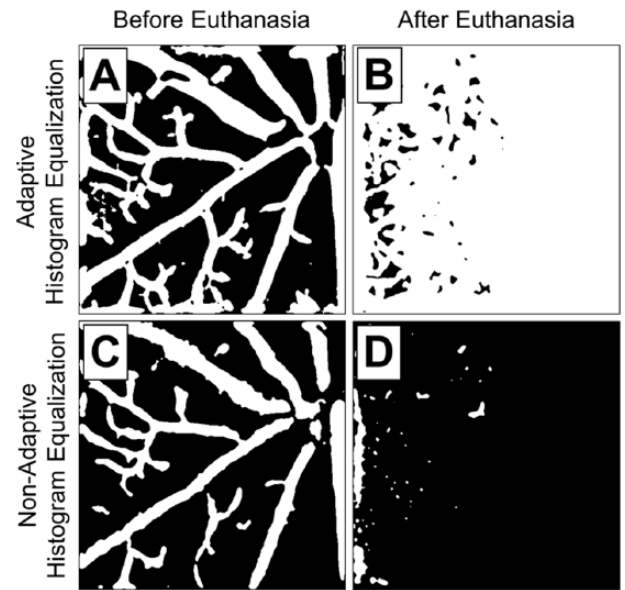


Figure 3. Binarized NFL en face images. Adaptive histogram equalization is biased toward the presence of a signal, as illustrated by sub-image (B) where the noise floor is interpreted as the presence of vasculature. Whereas a non-adaptive filter (C) does not detect every vessel that the adaptive approach detects (A), the non-adaptive approach more accurately depicts the absence of blood flow at time points where no blood flow exists (D). Image is representative of all 6 experiments. Field of view: $1.3\text{mm} \times 1.3\text{mm}$ ($37^\circ \times 37^\circ$). NFL, nerve fiber layer.

pre-euthanasia stage of the experiment (before isoflurane overdose was initiated). These averaged parameters were subsequently “hard-coded” to make a histogram equalization standard for each time point in the experiment. Histogram equalization removed the binarization algorithm’s bias toward the presence of blood flow and allowed comparison of early to late experimental time points (Figure 3). This “hard-coded” technique was reliable across each of the 6 experiments.

Blood flow volume fraction was calculated after vessel binarization by calculating the percentage of white pixels in the layer. Regional blood flow volume fraction by retinal region is then plotted versus time for each animal as a representation of animal death. At later time points, retinal layers became more difficult to discern; thus, blood flow volume fraction analysis was only performed in the superficial plexus (NFL). Once isoflurane overdose is initiated, blood flow volume fraction is expected to decrease to zero or the noise floor.

Total retinal thickness. Total retinal thickness is taken as the physical distance (μm) from the vitreous/ILM boundary to the ONL/RPE boundary. The refractive index of the retina was assumed to be 1.38 at 1310nm , based on a Conrady Dispersion²⁹ fit of Remtulla and Hallett’s³⁰ refractive index measurements. Changes in total retinal thickness can inform the retinal morphological status (eg, whether the retina swells or thins as the mouse expires). The retina is expected to become edematous as the mouse dies, and retinal edema should be detectable by SAR-OCT.

Reflectance index. Reflectance index has been demonstrated as an early indicator for glaucoma in non-human primates and humans.^{9,10} Here, reflectance index is defined as the ratio of mean intensity in the NFL to the mean intensity of the RPE, averaged over voxels in a plane perpendicular to the incident light direction (x - and y -direction)

$$\text{Reflectance index}(x, y) = \frac{\left[\frac{\sum_{z=T_{NFL}(x,y)}^{B_{NFL}(x,y)} I_{NFL}(x, y, z)}{H_{NFL}(x, y)} \right]}{\left[\frac{\sum_{z=T_{RPE}(x,y)}^{B_{RPE}(x,y)} I_{RPE}(x, y, z)}{H_{RPE}(x, y)} \right]} \quad (1)$$

where I is the intensity of a given voxel, T is the z -location of the top boundary of a layer, B is the z -location of the bottom boundary of a layer, and H is the total thickness of a layer. For this approach, both NFL and RPE were partially segmented—near the top boundary. Because of retinal degradation at later time points, only the most anterior 20 μm of both layers was considered. This ensures that the computed reflectance index includes only values from the NFL and RPE and does not artifactually extend into deeper retinal layers.

Scattering angle. Ratio processing of the SAR-OCT path lengths is a simple approach and was previously described by Wang et al.¹¹ Wang considered path length 3 which contains the highest angle scatterers and found that the average (en face) ratio of path length 1 to path length 3 (L/H_3) correlated with known azimuthal variation of RGC size.¹¹

To investigate utility of path length 2 in this study, histograms of the L/H_2 ratio for various retinal segments (eg, layers, quadrants, vasculature/non-vasculature regions) are compiled and examined instead of simple averages. Some retinal disease states, for example, may produce a relative increase in both high- and low-angle voxels and leave the average mostly unchanged.

The Burr Type XII distribution³¹ is used to parameterize normalized L/H histograms in any volumetric region of the murine retina. Distribution of L/H_2 values in the retina fit remarkably well to a Burr Type XII (or Burr) distribution as described in the Supplemental Material.

To detect temporal changes in scattering angle, histograms of the L/H_2 ratios are investigated over time by fitting to a Burr Type XII distribution and plotting the variation of the C parameter (a measure of distribution spread) over time. The C parameter variation is reported for 3 retinal layer groupings: (1) NFL + ganglion cell layer (GCL) + IPL, (2) INL + OPL + ONL, and (3) RPE + choriocapillaris (CC).

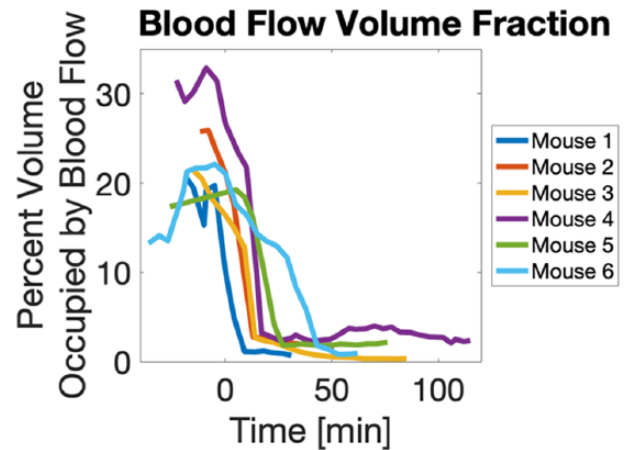


Figure 4. Blood flow volume fraction for each euthanized mouse plotted versus time, where $t=0$ minutes is the time at which isoflurane overdose was initiated. On average, the blood flow volume fraction began at 21.7% (± 6.385) and ended at 1.4% (± 0.824)—the noise floor. Average time from the initiation of isoflurane overdose to no blood flow (noise floor) was 20.5 minutes (± 12.582).

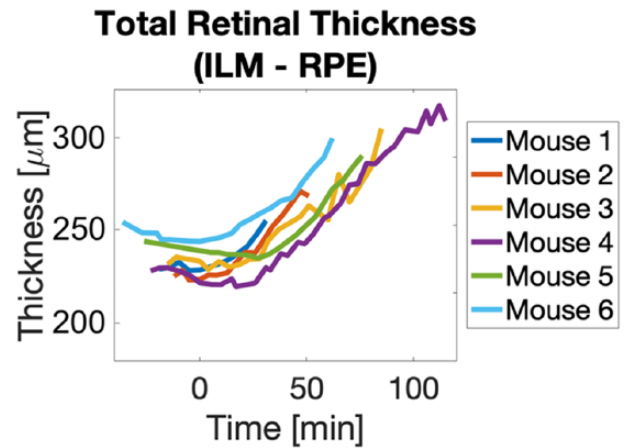


Figure 5. Total retinal thickness (ILM–RPE) increased after the initiation of isoflurane overdose from an average of 236.3 μm (± 11.30) at an average rate of 0.81 $\mu\text{m}/\text{min}$ (± 0.08). ILM, internal limiting membrane; RPE, retinal pigment epithelium.

Results

Results for each mouse participating in the study, for every feature, are presented (Figures 4 to 9) and described in the text following the figures.

Blood flow volume fraction

Blood flow volume fraction analysis for the superficial plexus revealed a decrease starting at the time isoflurane overdose was initiated ($t=0$ minutes). On average, the blood flow volume fraction began at 21.7% (± 6.385) and ended at 1.4% (± 0.824)—at the noise floor. Before isoflurane overdose, variation in the percent volume occupied by blood flow varied from 13% to 32% in the superficial plexus; this value was highly dependent on the region of interest (ROI) tracked during the

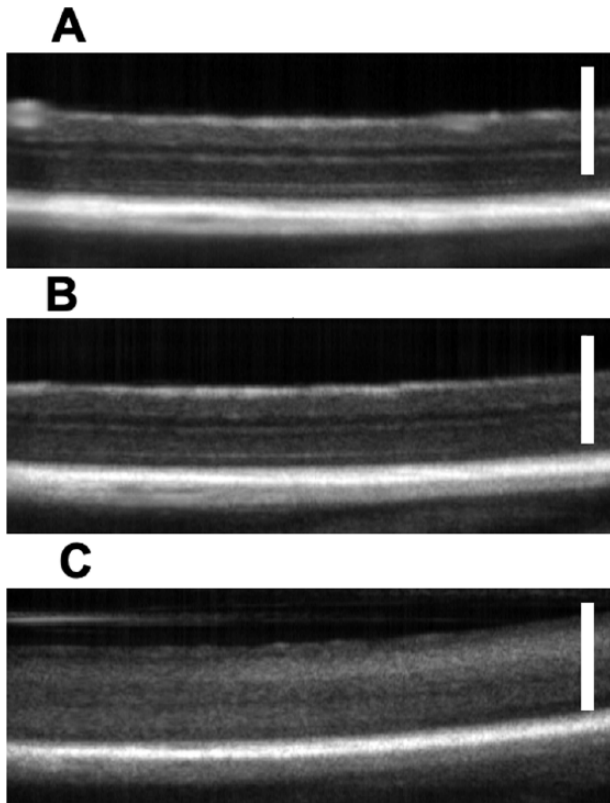


Figure 6. Total retinal thickness increases postmortem, and retinal layers become less distinct. The axial scale bars are 300 μm ; the lateral field of view is 1.3 mm (37°). (A) Mouse 3, -15 minutes, (B) mouse 3, 0 minutes, and (C) mouse 3, 45 minutes.

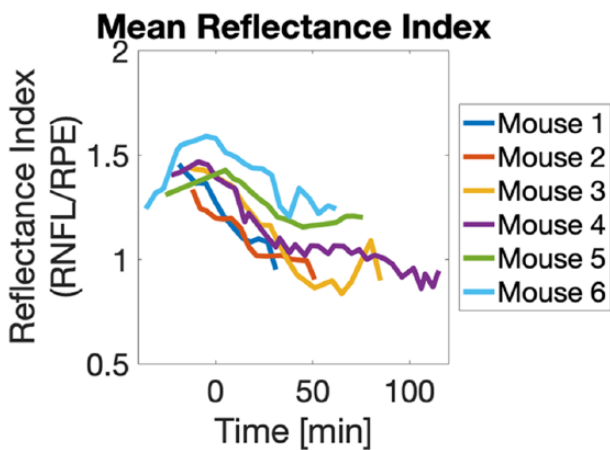


Figure 7. Mean reflectance index decreased after isoflurane overdose was initiated for each mouse. Decrease began before blood flow had ceased. In the case of mouse 6, reflectance increased up to around isoflurane overdose initiation. The average decrease in reflectance index occurred at a rate of -0.0056 [1/min] (± 0.0026).

ethanasia experiment. For some mice, the ROI was centered on the optic nerve head. This ROI maximized blood flow density in the image as vasculature density increases at the optic nerve head. For other mice, the ROI had the optic nerve head in the corner of the image, such that the vasculature density was lower. Mean time from isoflurane overdose to blood flow cessation was 20.5 minutes (± 12.582).

Total retinal thickness

Total retinal thickness (ILM–superficial boundary of the RPE) for each mouse before isoflurane overdose began averaged 236.3 ± 11.30 μm . For each mouse, total retinal thickness began to increase before blood flow ceased, and the retinal thickness increased approximately monotonically as long as the retina was reliably observable (before corneal clouding obscured the image). The average rate of thickness increase was 0.81 ± 0.08 $\mu\text{m}/\text{min}$. Example B-scans for mouse 3 are displayed (Figure 6).

Reflectance index

The reflectance index (NFL/RPE) decreased for every mouse. The average value of reflectance index at the initiation of isoflurane overdoses was 1.3775 ± 0.13 , and the average rate of decrease for reflectance index was -0.0056 ± 0.0026 [1/min]. Changes in reflectance index were not isolated to a single retinal region and were observed across all azimuthal regions.

Scattering angle

Representative L/H_2 distributions (mouse 2) for each layer grouping are shown (Figure 8). For every mouse and each retinal layer grouping (NFL + GCL + IPL, INL + OPL + OPL, RPE), distribution of L/H_2 values broadened during euthanasia. This distribution broadening is best captured by fitting the Burr Type XII distribution and reporting the C parameter values (Figure 9), which is a measure of variation. Before initiating euthanasia, the average C parameter value was 4.80 (± 0.21) for superficial layers, 4.84 (± 0.22) for intermediate layers, and 8.85 (± 0.35) for the RPE. At the time point where blood flow had ceased for each mouse, the C parameter mean values were 3.88 (± 0.15) for the superficial layers, 3.95 (± 0.23) for the intermediate layers, and 5.24 (± 0.53) for the RPE. A paired t -test showed significant differences between before and after the C parameter values in the superficial, intermediate, and deep retinal layers ($P = .00005$, $P = .0005$, and $P = .0002$, respectively). The C parameter decreased in every mouse by an average (\pm standard deviation) of 0.91 (± 0.18) for superficial layers, 0.90 (± 0.28) for intermediate layers, and 2.61 (± 0.62) for the RPE. Alpha and K parameters of the Burr Type XII distribution were not significantly different across layers or time.

Discussion

Blood flow volume fraction

A decrease in blood flow volume fraction was expected as the mouse expired. Canine distemper virus (CDV) detects movement in the tissue as it tracks voxels through time to magnify high-variance features. Voxels without movement appear whiter in the computed angiography image. As the heart function ceases, blood remains in the vessels but has less directed

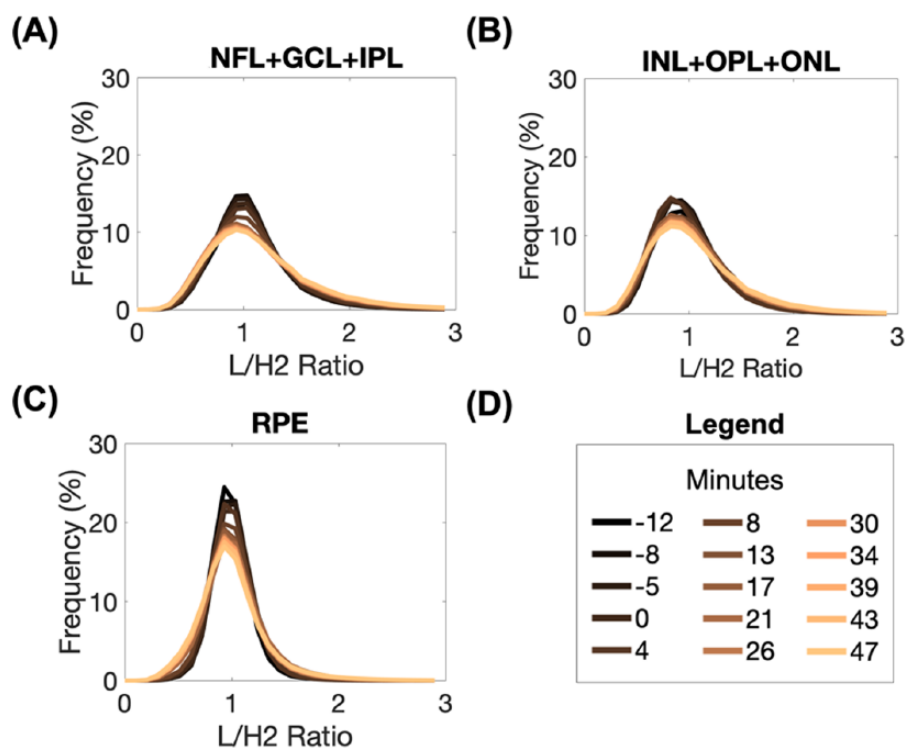


Figure 8. Example (mouse 2) distributions of L/H_2 values in (A) NFL + GCL + IPL, (B) INL + ONL + OPL, and (C) RPE layer groupings broaden over time. (D) The color legend for (A)-(C). The variation is captured by the C parameter of the Burr Type XII distribution. ILM, internal limiting membrane; INL, inner nuclear layer; IPL, inner plexiform layer; NFL, nerve fiber layer; ONL, outer nuclear layer; OPL, outer plexiform layer; RPE, retinal pigment epithelium.

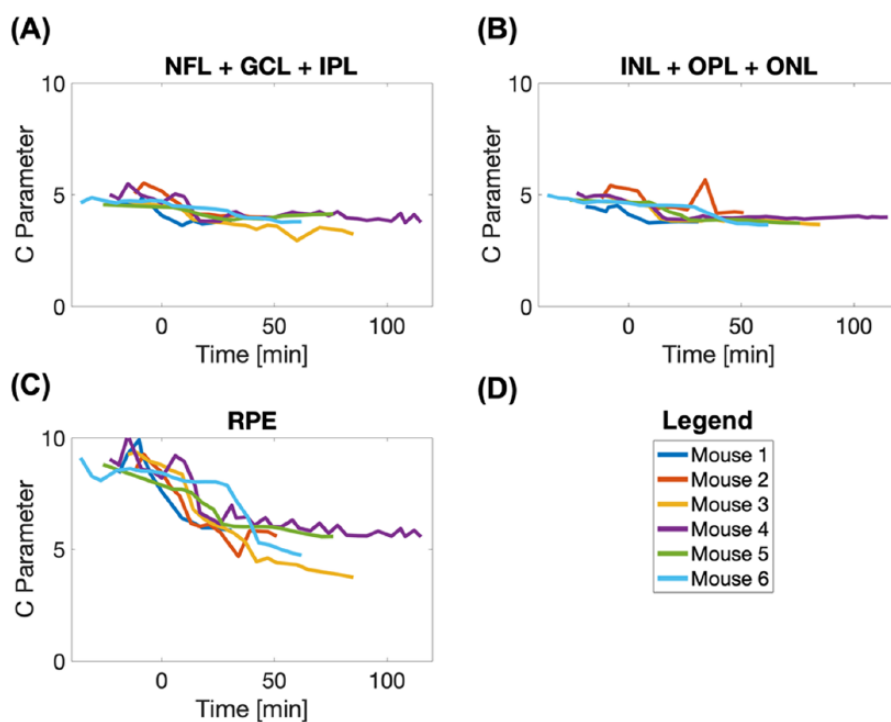


Figure 9. Burr Type XII distribution of the C parameter for (A) NFL + GCL + IPL, (B) INL + ONL + OPL, and (C) RPE layer groupings decreases over time for all mice after the initiation of isoflurane overdose. (D) The color legend for (A)-(C). ILM, internal limiting membrane; INL, inner nuclear layer; IPL, inner plexiform layer; NFL, nerve fiber layer; ONL, outer nuclear layer; OPL, outer plexiform layer; RPE, retinal pigment epithelium.

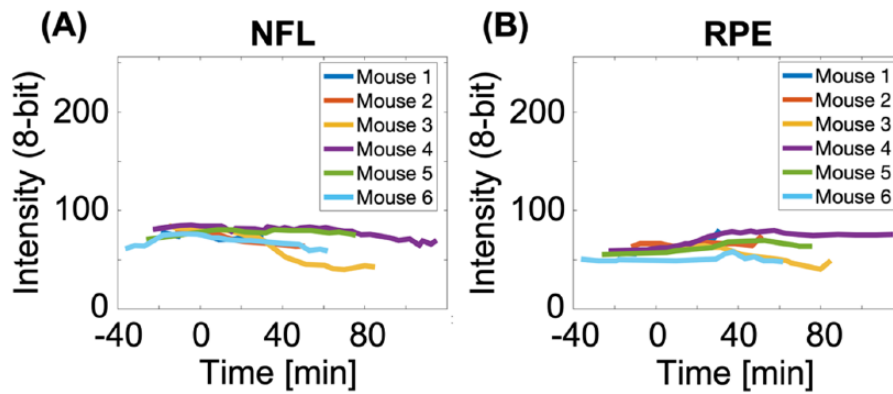


Figure 10. (A) The slight decrease in NFL intensity contributes to decreased reflectance index (equation (1)). (B) The slight increase in RPE intensity contributes to reflectance index decrease (equation (1)). NFL, nerve fiber layer; RPE, retinal pigment epithelium.

flow. Because the angiography method employed here is sensitive to Brownian motion, zero blood flow volume fraction may correspond to some blood coagulation. Small amplitude and random motion should persist beyond the directed flow resulting from the mouse's stroke volume. Some directed blood flow may exist even if the heartbeat is undetectable.

Total retinal thickness

Increase in total retinal thickness matched the expectation of edema in mice retinas. Retinal swelling suggests a movement of fluid to equalize osmotic gradients. Pannicke et al³² offer an osmotic explanation to retinal edema after induced ischemia in rat retinas. Their study suggests that ischemia-reperfusion of the rat retina over 10 minutes disrupts Kir4.1 channels at the blood-glial interface, which allows K⁺ ions to enter the glial cell interior, but not exit. Ions are accumulated in the glial cells which introduces a reverse osmotic gradient at the blood-glial interface. This gradient drives osmotic water movement (via AQP4 channels) from the blood into the glial cells and results in retinal edema.

Whereas tracking changes in thickness for each retinal sub-layer are of interest, the ability to distinguish each layer is diminished postmortem. Only retinal interfaces with large differences in refractive indices are apparent (eg, vitreous/ILM, ONL/RPE; Figure 6).

The significant increase in retinal thickness in the expired animals has implications for how and when histology is performed. Researchers involved in histological analysis of retinas should consider postmortem retinal swelling and aim to account for this effect. Perfusion fixation, if compatible with study design, may be a viable option for limiting artifacts due to swelling.

Reflectance index

The observed decrease in reflectance index while mice are deprived of oxygen is noteworthy. At least 2 mechanisms can

explain a decrease in reflectance index: a decrease in the NFL reflectivity or an increase in RPE reflectivity. In fact, both of these changes occur for each mouse studied: decreases in NFL reflectivity (Figure 10A) and increases in RPE reflectivity (Figure 10B). "Reflectivity" is the intensity of a particular retinal layer in the OCT image; variations in intensity could be due to variations in retinal scattering properties at 1.31 μ m.

Scattering angle

Although an increase or a decrease in reflectivity may not a priori be isolated to either changes in retinal absorption or scattering, SAR-OCT allows further analysis because the PME offers some angular discrimination. With SAR-OCT, a decrease in reflectance index is shown to be, at least in part, due to scattering angle changes. Thus, interesting results in this study are a combination of reflectance index increases and shifts in the L/H_2 distributions. In addition to the simple observation that the reflectivity index of the murine retina decreases as the animal expires, our results suggest that a shift in light scattering in the oxygen-deprived retina gives rise to the observed change.

For every layer, including both NFL and RPE, changes in the L/H_2 distributions reveal relative increases in both low- and high-angle scattering. That is, the probability of low-angle light scattering increases as the mouse expires ($L/H_2 > 1$ increases), and the probability of high-angle light scattering also increases ($L/H_2 < 1$ increases). The C parameter of the Burr Type XII distribution decreases for every layer.

As retinal tissue becomes more disorganized (entropy increases) and scattering patterns become more homogeneous, more light propagates to the RPE and a general decrease in the number of photons detected by the SAR-OCT system scattered from the NFL (Figure 10A). These photons can continue to travel deeper into the retina, which suggests that more photons can be transported to the RPE. Indeed, a higher number of photons are reflected from the RPE as the mouse expires (Figure 10B). Because of the simultaneous depth and angular

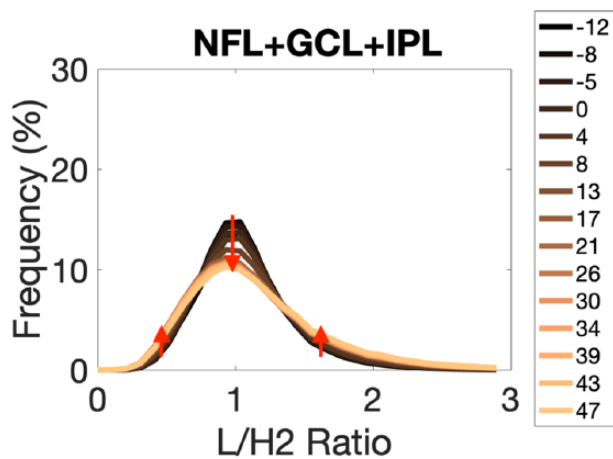


Figure 11. Burr Type XII distribution of L/H_2 in the NFL + GCL + IPL layer grouping for mouse 2 broadens through the euthanasia experiment. Arrows have been added to annotate the changes in the distribution from Figure 8(A). NFL, nerve fiber layer; IPL, inner plexiform layer.

discrimination available via SAR-OCT imaging, backscattering behaviors of both layers change in the same way giving a broader distribution of angles as the mouse expires.

Quantifying scattering diversity. Consider a superficial retinal volume with $512 \times 512 \times 10$ voxels. Each of these voxels has a measured L/H_2 value, usually between 0 and 3. For a healthy pre-euthanasia murine retina, the L/H_2 value tends to be around 1. In particular, about 15% of the voxels have an L/H_2 value that is between 0.95 and 1.05 (Figure 11; $t = -12$ minutes). For voxels with L/H_2 values around 1, the number of photons scattering at a low angle (path length 1) is about equal to the number of photons scattering at a high angle (path length 2). If N photons are detected in path lengths 1 and 2 (discounting path length 3) as having scattered from a voxel in the NFL where $L/H_2 = 1$, then we can say that $N/2$ photons are scattered at low angles and $N/2$ photons are scattered at high angles. For voxels in the NFL where L/H_2 values are between about 1.95 and 2.05 (about 2% of the voxels at $t = -12$ minutes; Figure 11), $2N/3$ photons were scattered at a low angle and $N/3$ photons were scattered at a high angle. The opposite is true for voxels in the NFL where the L/H_2 values are between 0.45 and 0.55: $N/3$ photons were scattered at a low angle and $2N/3$ photons were scattered at a high angle (about 3% of the voxels at $t = -12$ minutes; Figure 11).

As the mouse expires, the probability that any given voxel in the NFL scatters such that $N/2$ photons are scattered at low angles and $N/2$ photons are scattered at high angles ($0.95 < L/H_2 < 1.05$) decreases from 15% to 10% at $t = 47$ minutes (Figure 11). At the same time, the probability that any given voxel in the NFL scatters such that $2N/3$ photons scatter at low angles and $N/3$ photons scatter at high angles ($1.95 < L/H_2 < 2.05$) increases from 2% to 3%. Similarly, the probability that any given voxel in the NFL scatters such that $N/3$ photons scatter at low angles and

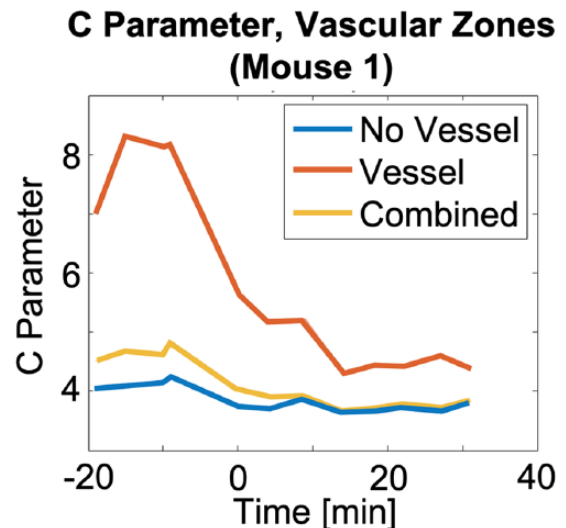


Figure 12. The C parameter in retinal zones with more (orange) and less (blue) vascular area fraction.

$2N/3$ photons scatter at high angles ($0.45 < L/H_2 < 0.55$) increases from around 3% to around 4%. The same trend holds for voxels in the RPE.

Scattering and vascular tissue. To explore the contribution of vascular versus neural tissue to the observed scattering angle changes, a blood vessel mask was applied for this analysis. The vascular images obtained by OCT angiography, using the non-adaptive filtering technique, create 2 vascular zones: areas of the retina with a greater fraction of blood volume and areas with lesser blood volume. To provide clarity on the source of scattering angle changes, the C parameter was evaluated in both of these regions in the NFL for mouse 1. Results suggest that, indeed, changes in blood volume do contribute significantly to a decrease in the C parameter. A smaller decrease in the C parameter is also observed in the less vascular regions of the retina (Figure 12). Murine retinal vascular changes significantly affect the C parameter. We note that those voxels labeled as less vascular in fact contain smaller vascular structures (capillaries) that went undetected by OCT angiography.

The major contribution of the vasculature to changes in the C parameter deserves further study. Although several biological mechanisms are recognized that could produce changes in the retinal vasculature that are consistent with the observations, none of them are within the scope of this study; further studies involving SAR-OCT should explore specific biological mechanisms of scattering angle changes in the hypoxic retinal vasculature.

The authors note that the C parameter for mouse 1 (Figure 12) begins to decrease before initiation of euthanasia. The plot for mouse 1 in Figure 4 confirms that the blood flow remained unaffected until after the 0-minute mark when euthanasia was initiated. The result suggests that the cause of the observed C parameter decrease is not associated

exclusively with blood flow, but is closely connected to vascular changes.

Results of the study suggest that in the hypoxic murine retina both high- and low-angle scattering increases relative to the more balanced backscattering exhibited by healthy mice. This increase in scattering angle diversity is detected by the C parameter enabled by SAR-OCT; as the scattering angle diversity increases, the C parameter decreases.

Future work

This study was directed to investigate longitudinal scattering angle changes which may be detected volumetrically using SAR-OCT. This is the first report describing longitudinal changes in light backscattering angles in the retina using SAR-OCT. However, this study alone does not necessarily confirm the utility of SAR-OCT for more subtle changes in the scattering properties of the retina, as the hypoxic insult examined was severe (euthanasia). The observed increase in scattering angle diversity of the retina is related to the cessation of blood flow, but more studies are needed to investigate mechanisms giving rise to changes in scattering angle from the vasculature and if these changes are observable in more realistic disease models. Results of the studies suggest that SAR-OCT is a candidate imaging method for the detection of retinal neuropathies.

Conclusions

In total, 6 mice were euthanized and their retinas imaged with SAR-OCT for approximately 90 minutes until each animal expired. Decreases in volumetric blood flow volume fraction provided an indicator of tissue perfusion during the hypoxic insult. For all animals studied, total retinal thickness increased and reflectance index decreased. Most strikingly, the distribution of L/H_2 values showed a distinct broadening pattern, indicating an increase in both high- and low-angle scattering when compared with the initial state of the mouse, pre-euthanasia. A major effect on scattering angle distribution was observed in voxels containing blood vessels. SAR-OCT is sensitive to longitudinal alterations in scattering properties of the murine retina during a hypoxic insult.

Author Contributions

MRG, HGR III, and TEM- Conceptualization, MRG, HGR III, and TEM-methodology, MRG and ASR-software, MRG-validation, MRG-formal analysis, MRG-investigation, HGR III and TEM-resources, MG and HGR III-data curation, MRG- writing-original draft preparation, MRG, HGR III, and TEM- writing-review and editing, MRG-visualization, HRG and TEM-supervision, HGR III and TEM-project administration, HGR III and TEM- funding acquisition.

Supplemental Material

Supplemental material for this article is available online.

ORCID iDs

Michael R Gardner  <https://orcid.org/0000-0002-2308-0707>

REFERENCES

1. Watson C, Paxinos G. *Chemoarchitectonic Atlas of the Mouse Brain*. Cambridge, MA: Academic Press; 2010.
2. Zonner SW, Ejima K, Fulgar CC, et al. Oculomotor response to cumulative sub-concussive head impacts in US high school football players: a pilot longitudinal study [published online ahead of print December 20, 2018]. *JAMA Ophthalmol*. doi:10.1001/jamaophthalmol.2018.6193.
3. Elbin RJ, Sufrinko A, Anderson MN, et al. Prospective changes in vestibular and ocular motor impairment after concussion. *J Neurol Phys Ther*. 2018;42:142–148.
4. McKee AC, Alosco ML. Assessing subconcussive head impacts in athletes playing contact sports—the eyes have it [published online ahead of print December 20, 2018]. *JAMA Ophthalmol*. doi:10.1001/jamaophthalmol.2018.6199.
5. Hines-Beard J, Marchetta J, Gordon S, Chaum E, Geisert EE, Rex TS. A mouse model of ocular blast injury that induces closed globe anterior and posterior pole damage. *Exp Eye Res*. 2012;99:63–70.
6. Mohan K, Kecova H, Hernandez-Merino E, Kardon RH, Harper MM. Retinal ganglion cell damage in an experimental rodent model of blast-mediated traumatic brain injury. *Invest Ophthalmol Vis Sci*. 2013;54:3440–3450.
7. Vien L, DalPorto C, Yang D. Retrograde degeneration of retinal ganglion cells secondary to head trauma. *Optom Vis Sci*. 2017;94:125–134.
8. Mostafa J, Wickum S, Frishman LJ, Porter J. Retinal abnormalities in patients with different severities of traumatic brain injury. *Invest Ophthalmol Vis Sci*. 2017;58:5647.
9. Dwelle J, Liu S, Wang B, et al. Thickness, phase retardation, birefringence, and reflectance of the retinal nerve fiber layer in normal and glaucomatous non-human primates. *Invest Ophthalmol Vis Sci*. 2012;53:4380–4395.
10. Liu S, Wang B, Yin B, et al. Retinal nerve fiber layer reflectance for early glaucoma diagnosis. *J Glaucoma*. 2014;23:e45–e52.
11. Wang B, Yin B, Dwelle J, Rylander HG III, Markey MK, Milner TE. Path-length-multiplexed scattering-angle-diverse optical coherence tomography for retinal imaging. *Opt Lett*. 2013;38:4374–4377.
12. Gardner MR, Katta N, McElroy A, Baruah V, Rylander HG, Milner TE. Scattering angle resolved optical coherence tomography for in vivo murine retinal imaging. In: *SPIE Bios International Society for Optics and Photonics*. Bellingham, WA: SPIE; 2017:1005310.
13. Gardner M, Katta N, Rahman A, Rylander H, Milner T. Design considerations for murine retinal imaging using scattering angle resolved optical coherence tomography. *Appl Sci*. 2018;8:2159.
14. Kamp MA, Sarikaya-Seiwert S, Petridis AK, et al. Intraoperative indocyanine green-based cortical perfusion assessment in patients suffering from severe traumatic brain injury. *World Neurosurg*. 2017;101:431–443.
15. Jian Y, Zawadzki RJ, Sarunic M. Adaptive optics optical coherence tomography for in vivo mouse retinal imaging. *J Biomed Opt*. 2013;18:56007.
16. Jian Y, Xu J, Gradowski MA, Bonora S, Zawadzki RJ, Sarunic M. Wavefront sensorless adaptive optics optical coherence tomography for in vivo retinal imaging in mice. *Biomed Opt Express*. 2014;5:547–559.
17. Zhang P, Mucci J, Wahl DJ, et al. Effect of a contact lens on mouse retinal in vivo imaging: effective focal length changes and monochromatic aberrations. *Exp Eye Res*. 2018;172:86–93.
18. McLenachan S, Magno AL, Ramos D, et al. Angiography reveals novel features of the retinal vasculature in healthy and diabetic mice. *Exp Eye Res*. 2015;138:6–21.
19. Zhi Z, Yin X, Dziennis S, et al. Optical microangiography of retina and choroid and measurement of total retinal blood flow in mice. *Biomed Opt Express*. 2012;3:2976–2986.
20. Alnawaiseh M, Rosentreter A, Hillmann A, et al. OCT angiography in the mouse: a novel evaluation method for vascular pathologies of the mouse retina. *Exp Eye Res*. 2016;145:417–423.
21. Yi J, Wei Q, Liu W, Backman V, Zhang HF. Visible-light optical coherence tomography for retinal oximetry. *Opt Lett*. 2013;38:1796–1798.
22. Chen S, Shu X, Yi J, Fawzi AA, Zhang HF. Dual-band optical coherence tomography using a single supercontinuum laser source. *J Biomed Opt*. 2016;21:66013.
23. Fialova S, Augustin M, Glosmann M, et al. Polarization properties of single layers in the posterior eyes of mice and rats investigated using high resolution polarization sensitive optical coherence tomography. *Biomed Opt Express*. 2016;7:1479–1495.
24. Augustin M, Fialova S, Himmel T, et al. Multi-functional OCT enables

- longitudinal study of retinal changes in a VLDLR knockout mouse model. *PLoS ONE*. 2016;11:e0164419.
25. Yin B, Dwelle J, Wang B, et al. Fourier optics analysis of phase-mask-based path-length-multiplexed optical coherence tomography. *J Opt Soc Am A Opt Image Sci Vis*. 2015;32:2169–2177.
 26. Pratt WK. *Digital Image Processing*. New York, NY: John Wiley & Sons, Inc; 1978.
 27. Nam AS, Chico-Calero I, Vakoc BJ. Complex differential variance algorithm for optical coherence tomography angiography. *Biomed Opt Express*. 2014;5:3822–3832.
 28. Frangi AF, Niessen WJ, Vincken KL, Viergever MA. Multiscale vessel enhancement filtering. In: *International Conference on Medical Image Computing and Computer-Assisted Intervention*. New York, NY: Springer; 1998:130–137.
 29. Conrady AE. *Applied Optics and Optical Design, Part Two* (ed. R Kingslake), 1st ed. New York, NY: Dover Publications, Inc; 1960.
 30. Remtulla S, Hallett PE. A schematic eye for the mouse, and comparisons with the rat. *Vision Res*. 1985;25:21–31.
 31. Singh SK, Maddala GS. A function for size distribution of incomes. In: Chotikapanich D, ed. *Modeling Income Distributions and Lorenz Curves*. New York, NY: Springer; 2008:27–35.
 32. Pannicke T, Iandiev I, Uckermann O, et al. A potassium channel-linked mechanism of glial cell swelling in the postischemic retina. *Mol Cell Neurosci*. 2004;26:493–502.